Southern Ocean CO2 release at the peak warmth of the Cenozoic

Simone Moretti

simone.moretti@mpic.de

Max Planck Institute for Chemistry https://orcid.org/0000-0002-6772-7269

François Fripiat

Université Libre de Bruxelles https://orcid.org/0000-0002-2591-6301

Mathis Hain

University of California, Santa Cruz https://orcid.org/0000-0002-8478-1857

Valeria Luciani

Università di Ferrara

Lucas Lourens

Faculty of Geosciences, Utrecht University https://orcid.org/0000-0002-3815-7770

Paul Paul Borucki

Johannes Gutenberg University

Lukas Gerber

Heidelberg University https://orcid.org/0009-0008-8721-6889

Tobias Agterhuis

Utrecht University

Laura Haynes

Vassar College https://orcid.org/0000-0003-1914-3282

Giulia Filippi

Università di Ferrara https://orcid.org/0000-0002-0304-8830

Ralf Schiebel

Max Planck Institute for Chemistry

Gerald Haug

Max Planck Institute for Chemistry

Daniel Sigman

Princeton University https://orcid.org/0000-0002-7923-1973

Alfredo Martinez-Garcia

Max Planck Institute for Chemistry https://orcid.org/0000-0002-7206-5079

Article

Keywords:

Posted Date: October 9th, 2025

DOI: https://doi.org/10.21203/rs.3.rs-6622599/v1

Additional Declarations: There is **NO** Competing Interest.

Southern Ocean CO_2 release at the peak warmth of the Cenozoic

Simone Moretti[1,2] *, François Fripiat[3], Mathis P. Hain[4], Valeria Luciani[5], Lucas Lourens[6], Paul Borucki[7], Lukas Gerber[8], Tobias Agterhuis[6], Laura Haynes[9], Giulia Filippi[5], Ralf Schiebel[1], Gerald H. Haug[1,10], Daniel M. Sigman[11], Alfredo Martínez-García[1]*

Affiliations:

[1] Climate Geochemistry Department, Max Planck Institute for Chemistry, Mainz, Germany

[2] Istituto di Scienze Polari, Consiglio Nazionale delle Ricerche, Bologna, Italy

[3] Department Geosciences, Environment and Society, Université libre de Bruxelles, Brussels, Belgium

[4] Department of Earth and Planetary Sciences, University of California, Santa Cruz, Santa Cruz, United States

[5] Dipartimento di Fisica e Scienze della Terra, Università di Ferrara, Ferrara, Italy

[6] Department of Earth Sciences, Utrecht University, Utrecht, Netherlands

[7] Institut für Geowissenschaften, Johannes Gutenberg University, Mainz, Germany

[8] Institut für Geowissenschaften, University of Heidelberg, Heidelberg, Germany

[9] Department of Earth Science and Geography, Vassar College, Poughkeepsie, United States

[10] Department of Earth Sciences, ETH Zurich, Zurich, Switzerland

[11] Department of Geosciences, Princeton University, Princeton, United States

*Correspondence to: simone.moretti@mpic.de or a.martinez-garcia@mpic.de

The Early Eocene Climatic Optimum (EECO) was an interval in Earth's history when reconstructed temperatures and atmospheric CO_2 concentrations were among the highest of the Cenozoic Era (i.e., the last 66 million years)[1]. The causes of the high CO_2 levels remain unclear[2]. The Southern Ocean, a major "leak" in the global ocean's biological carbon pump that has been implicated in the CO_2 changes over recent ice age cycles[3], may also have played a role earlier in the Cenozoic. Here, we report foraminifera-bound $\delta^{15}N$ measurements that show higher surface nitrate concentrations in the Southern Ocean during peak EECO. The associated venting of CO_2 from the deep ocean to the atmosphere would have been amplified by the low seawater *p*H buffering capacity of the Eocene. Previously proposed low silicate rock weatherability during the Eocene[4,5] may have weakened the "weathering thermostat", allowing the reconstructed change in

biological pump efficiency in the Southern Ocean to explain at least half of the atmospheric CO_2 increase observed during the EECO.

While no known analogue in Earth's climate history exists to match the rates of ongoing warming, our planet has experienced much warmer periods in its past[1,6]. One of the warmest intervals of the Cenozoic was the Early Eocene Climate Optimum (EECO), with peak temperature between approximately 53 to 49 million years ago. The exceptionally high temperatures of the EECO were matched by the highest atmospheric CO_2 concentrations of the Cenozoic, reaching ~1600 ppm[1]. Thus, the EECO provides a valuable case study for evaluating the accuracy of numerical simulations in estimating the equilibrium climate response to high atmospheric CO_2[7]. While the progressive decline in atmospheric CO_2 since the early Cenozoic has been linked to changes in the fluxes of carbon and alkalinity between geologic reservoirs and the ocean-land-atmosphere system[8,9] via the silicate rock weathering feedback[10,11], the mechanisms causing peak EECO CO_2 are debated. Previously proposed drivers include decreased organic carbon burial[12], continental rifting[13], continental arc volcanism with associated metamorphic decarbonation[14], CO_2 release from large igneous provinces[15,16], subduction of tropical pelagic carbonates under the Asian plate and their volcanic recycling as CO_2[17]. However, temporal lags between evidence of volcanism and warming[18] and numerical simulations[2] suggest that these sources alone cannot explain the highest levels of CO_2 reconstructed during the EECO.

The ocean's biological carbon pump stores CO_2 in excess of saturation in the voluminous ocean's interior, lowering the concentration of CO_2 in the atmosphere[19,20]. The CO_2 sequestration capacity of the ocean's biological pump is affected by the degree to which phytoplankton use the available nutrients in the high latitude ocean surface[21]. Today, the biological pump operates below its maximum potential, mainly due to the ventilation of the deep ocean from the Southern Ocean, where upwelled nutrients (and an associated excess of CO_2) are not fully consumed by phytoplankton[20,22].

The stable isotopes of nitrogen (N) track the degree of seasonal nitrate (NO_3^-) drawdown in the Southern Ocean surface. Phytoplankton preferentially assimilate ^{14}N into organic matter, leaving the residual surface NO_3^- pool enriched in ^{15}N, a process that in Antarctic surface waters can be approximated with Rayleigh fractionation kinetics[23,24]. As NO_3^- is progressively consumed, there is an increase in the $\delta^{15}N$ of NO_3^- and the plankton growing on that NO_3^- ($\delta^{15}N$

$= (^{15}N/^{14}N)_{sample} / (^{15}N/^{14}N)_{air} - 1$), with the integrated assimilated N ($\delta^{15}N_{SO}$) approaching the $\delta^{15}N$ of the deep-sourced NO_3^- supply ($\delta^{15}N_{deep}$) as the NO_3^- supply reaches complete consumption (Methods). Foraminifera bound $\delta^{15}N$ (hereafter FB-$\delta^{15}N$), provides a tool to reconstruct past changes in the degree of NO_3^- consumption, as the $\delta^{15}N$ of organic matter protected by and preserved in the calcite of foraminifera shell matrix reflects the $\delta^{15}N$ of their diet and thus the average $\delta^{15}N$ of nitrate converted to plankton biomass in the surface ocean[25,26].

Fossil-bound $\delta^{15}N$ indicates enhanced nutrient drawdown in the Southern Ocean during the Pleistocene ice ages, working to increase the efficiency of the global ocean's biological pump during cold glacial periods[27–29]. This has been proposed as a central cause of the lower atmospheric CO_2 concentrations during the late Pleistocene glaciations[30,31]. However, the specific application of FB-$\delta^{15}N$ as a tracer of nutrient drawdown over longer timescales is complicated by the shifting baseline in $\delta^{15}N_{deep}$, which has changed substantially over the Cenozoic[32–34].

Here, we report measurements of FB-$\delta^{15}N$ of four sediment cores collected by the Ocean Drilling Program (ODP) that cover the EECO with sufficient stratigraphic resolution (Methods). These include mid-latitude Atlantic and Indian Ocean Sites 1263 and 762, respectively, and Antarctic Southern Ocean Sites 690 and 738 (Fig. 1). A stack of FB-$\delta^{15}N$ data from mid-latitude ocean Sites 1263 and 762 (FB-$\delta^{15}N_{ML}$) provides an estimate of $\delta^{15}N_{deep}$, as follows. In these oligotrophic regions, nitrate consumption is nearly complete, and FB-$\delta^{15}N$ reflects the $\delta^{15}N$ of NO_3^- supply from the underlying pycnocline (roughly the upper 1.2 km)[25]. The pycnocline, in turn, tracks budgetary changes in the global N cycle[35], which ultimately drive the global FB-$\delta^{15}N$ signal that is shared among all sites (Fig. 2d; Methods). Thus, the FB-$\delta^{15}N$ records from the mid-latitude sites, when taken together (FB-$\delta^{15}N_{ML}$), record changes in global ocean nitrate $\delta^{15}N$ ($\delta^{15}N_{deep}$) through time. In order to reconstruct the Southern Ocean nutrient status changes across the EECO, a stack of the Southern Ocean FB-$\delta^{15}N$ records from Sites 690 and 738 (FB-$\delta^{15}N_{SO}$) is differenced from FB-$\delta^{15}N_{ML}$ at interpolated time steps (hereafter $\Delta\delta^{15}N_{SO\text{-}ML}$) (Fig. 2c), in order to reconstruct the Southern Ocean nutrient status changes across the EECO. The resulting estimate of changes in the degree of NO_3^- consumption (Δf) is used as input for an ocean-atmosphere box model to quantify its expected effect on atmospheric CO_2.

Higher surface nitrate in the Southern Ocean during the EECO

The global ocean nitrogen cycle responded to the strong warming during the EECO, with a reduction of water column denitrification that caused a large decrease in whole-ocean NO_3^- $\delta^{15}N$ and thus FB-$\delta^{15}N$[32], as recorded in all sites of our compilation, with a long-term decline in FB-$\delta^{15}N$ from ~12 ‰ to 5‰ (Fig. 2d). Despite this global ocean change, the Southern Ocean sites 690 and 738 are consistently lower in FB-$\delta^{15}N$ than coeval mid-latitude sites 1263 and 762, a trend that is the most pronounced during the EECO (Fig. 2d). While this feature is expressed individually in both the Atlantic and Indian basins, it is generalized across basins by $\Delta\delta^{15}N_{SO\text{-}ML}$ (Fig. 2b). Our estimation of changes in $\Delta\delta^{15}N_{SO\text{-}ML}$ (and thus nutrient consumption) is conservative, as we make use of Site 762 for the mid-latitude stack, even if it shows intermediate $\delta^{15}N$ values between high latitude sites 690 and 738 and mid-latitude Site 1263, reducing the amplitude of the signal. The maximum amplitude of this gradient ($\Delta\delta^{15}N_{SO\text{-}ML}$) coincides with the EECO maxima in temperature and atmospheric CO_2 concentration (Fig. 2a; Fig. 3a). Before and after the EECO, this gradient weakens or disappears, reflecting that the FB-$\delta^{15}N_{SO}$ is similar to FB-$\delta^{15}N_{ML}$. We argue that the observed EECO maximum in $\Delta\delta^{15}N_{SO\text{-}ML}$ points to a decline in the degree of Southern Ocean NO_3^- consumption, leaving more NO_3^- unused in the surface so as to reduce ocean carbon storage by the biological pump.

We use the Rayleigh model to quantitatively estimate changes in the degree of NO_3^- consumption (Δf) in the Southern Ocean, based on field estimates for the isotope effect of nitrate assimilation[24]. The calculated value of Δf over the EECO (Fig. 3b) suggests a ~40% decline in the degree of nutrient consumption in the Southern Ocean during peak EECO temperature and CO_2. This decrease in degree of NO_3^- consumption was due to either an increase in circulation- and mixing-driven nutrient supply to the surface ocean or a decline in phytoplankton growth and the associated export of sinking organic matter from the Southern Ocean surface to the interior. We consider these two options below.

Mechanisms of deep ocean ventilation by the Southern Ocean

Geochemical data indicate that the Southern Ocean was the dominant source of the global ocean's deep water during the Paleogene[36,37]. This is supported by numerical simulations, in which the shallow/closed Drake and Tasmanian Passages support a western boundary current, facilitating the southward advection of warm, salty water from the subtropics into subpolar

gyres, resulting in a large Southern Ocean overturning cell with deep water formation near Antarctica[38,39]. Our observation of less complete NO_3^- consumption during the EECO in this deep ocean-ventilating region implies a shift from regenerated to preformed nutrients in the ocean interior[20], reducing the efficiency of the global ocean's biological pump by allowing biologically sequestered CO_2 to escape to the atmosphere.

Support for our findings comes from reduced vertical carbon isotope gradients observed in a global planktic and benthic foraminifera EECO compilation, which has been interpreted to reflect reduced biological pump efficiency[40] (Fig. 3d). The associated decrease in the storage of respired CO_2 in the ocean interior should have increased its oxygen (O_2) concentration, countering the effect of lower O_2 solubility in warmer ocean water. Supporting evidence for enhanced ventilation during the EECO includes the contraction of oxygen deficient zones in the Pacific[32,33] and the demise of low oxygen-dwelling foraminifera taxon *Chiloguembelina* in the Atlantic and Indian Oceans[41]. Additional support for enhanced overturning during the EECO is found in the collapse of planktic-benthic $\delta^{18}O$ difference in Southern Ocean Sites 738 and 690, which may indicate reduced surface-deep density difference, enhanced vertical mixing, and Southern-sourced deep ocean ventilation[33] (Fig. 3c). Finally, during the EECO, high-latitude Southern Ocean nannofossil assemblages shifted toward colder and nutrient-rich dwelling taxa[42].

The weakening of the biological pump associated with EECO warming mirrors patterns observed during the warm interglacial periods that interrupt the Pleistocene ice ages[3]. Interglacials are characterized by enhanced nutrient upwelling to the Southern Ocean surface[29], increased deep ocean oxygen concentration[43], and a reduced vertical carbon isotope gradient[44], all indicative of lower biological pump efficiency under warmer climatic conditions. Thus, the Pleistocene interglacials and the EECO, when taken together, point to a consistent response of Southern Ocean nutrient repletion to warming across different timescales. Regardless of the underlying mechanisms, this process generates a positive feedback loop between Southern Ocean ventilation, atmospheric CO_2, and global mean temperature. While this feedback has been proposed to operate at the glacial-interglacial timescale[45], our findings suggest it may also be active on much longer timescales such as during the EECO.

Strengthening and southward displacement of South Westerly Winds (SWW) has been proposed as a mechanism to explain a more vigorously mixed Southern Ocean and higher

nutrient supply at the end of glacial periods[3,45,46], a trend that is expected to continue under future warming[47]. This wind-driven circulation in the polar regions would shorten the residence time of surface waters and thus reduce the potential for the excess precipitation relative to evaporation to form a halocline, setting the stage for deep convection in the winter[45,48]. Climate warming may also be associated with strengthening and poleward displacement of the westerlies in the Northern Hemisphere[49], with an effect on the circulation in the subpolar gyres. A second and complementary mechanism to enhance deep ocean mixing from the Southern Ocean relates to seawater density becoming more sensitive to seasonal temperature changes as the ocean warms overall, with winter cooling driving deeper convection, stronger winter mixing and enhanced nutrient supply from the subsurface ocean[50–53]; as has been considered as a mechanism of polar ocean stratification in colder climates on glacial-interglacial and Plio-Pleistocene timescales[50,51].

As a possible alternative to an increase in Southern Ocean overturning during the EECO, a decline in biological productivity would also work to explain the reconstructed rise in unconsumed nutrients in the Southern Ocean surface, weakening the efficiency of the biological pump so as to raise atmospheric CO_2. Presently, productivity in the Southern Ocean is limited by iron[54], the increased supply of which has led to increased nutrient drawdown in the subantarctic zone of the Southern Ocean, thereby lowering CO_2 during Pleistocene ice ages[27]. However, the leverage of iron on Southern Ocean productivity and nutrient consumption may require the colder climatic conditions of the Pleistocene, through greater aridity and continental erosion rates[55]. Therefore, changes in the vertical supply of nutrients appear the most feasible explanation for enhanced nutrient repletion in the Southern Ocean during the EECO. The mechanism aside, a rise in Antarctic surface nutrients indicate a reduced biological pump efficiency and, thus, net CO_2 outgassing from the ocean, during the EECO.

Effect of the Southern Ocean on the Eocene carbon cycle

The response of atmospheric CO_2 to changes in the degree of polar ocean nutrient consumption (Δf) is commonly framed in terms of change in the ocean's regenerated nutrient content (ΔN_{reg}) and its associated respired carbon storage. Theory and numerical models suggest that linear change in N_{reg} causes an exponential change in CO_2[20,56], with the slope of the relationship determined by the stoichiometry of phytoplankton biomass (R term) and background seawater buffering ($CPF/[CO_3^{2-}]$ term)[9,57] :

$$\Delta_f lnCO_2 \approx \frac{CPF}{[CO_3^{2-}]} * (R_{C:N} - R_{ALK:N}) * \Delta N_{reg} \approx k * \overline{N} * \Delta f \quad (1)$$

To illustrate the consequence of these sensitivities, we adopt the box model of Sarmiento & Toggweiler[21] and compare simulated CO_2 changes for a reduction in Southern Ocean nutrient consumption under idealized preindustrial and Eocene conditions, assuming that the ocean's overall nutrient inventory $\overline{N}$ was constant. Relative to the preindustrial, the Eocene scenario is initialized with elevated CO_2 of 700 ppm[1] yielding 7˚C warming, with elevated Eocene seawater Ca^{2+} yielding reduced seawater carbonate ion concentration and buffering[9], but with the same calcite saturation depth (CSH) of 3000 m (Fig. 4). The CO_2 effects of changes in Southern Ocean nutrient consumption (Δf) are evaluated under three conditions: i) closed system with constant DIC, ALK and temperature (T), where steady state CSH is changing, ii) the same closed system experiment but with CO_2-induced change in T that causes further carbon system changes (Extended Data Fig. 5 & 6), and iii) the same T-feedback experiment but with an open system "$CaCO_3$ compensation" feedback that maintains the depth of the CSH [31,58,59].

In all scenarios, the same Δf causes a nearly linear change in $lnCO_2$, which translates to much larger absolute CO_2 change under the elevated baseline CO_2 of the EECO (Fig. 4), mainly due to the reduced CO_3^{2-} buffering of Eocene seawater[9]. The temperature and carbonate compensation feedbacks act to amplify simulated CO_2 change by lowering the solubilities of both CO_2 and $CaCO_3$ to drive further ocean alkalinity reduction, CO_2 rise and warming, together yielding a network of mutually amplifying feedbacks that increase the sensitivity of CO_2 to Δf (Fig. 4). In our simple numerical model, the reconstructed EECO reduction in nutrient consumption ($\Delta f = -0.4$) raises CO_2 from an initial concentration of 700ppm to 900ppm without feedbacks and to 1100ppm when including carbonate compensation and temperature feedbacks, explaining at least half of the ~800 ppm CO_2 rise reconstructed for the EECO[1] (Fig. 4).

On the million-year timescale, the chemical weathering of silicate rocks stabilizes Earth's climate through CO_2 drawdown[57]. In the conventional silicate weathering paradigm[10], any CO_2 release from the Southern Ocean would lead to warming and silicate weathering in excess of geologic CO_2 sources, so that CO_2 and climate are restored over an e-folding timescale of less than one million years[57,60], thus reducing or preventing the atmospheric CO_2 effect of the biological pump over the ~4 million year duration of the EECO. However, recent work suggests

that reduced global-scale weatherability and weathering sensitivity to climate may have interfered with the silicate weathering feedback during the early Cenozoic. The lack of mountain building and the peneplain continental configuration during the Early Eocene, prior to the uplift of the Alpine-Himalayan belt, may have reduced the supply of fresh rock to the critical zone of silicate weathering[11], consistent with high early Cenozoic weathering intensity reconstructed from marine carbonate lithium isotopes (δ^7Li)[4] (Fig. 3a). In deeply weathered soils, slow flushing of weathering products reduces dissolution rates of primary silicate minerals[61] and favors the precipitation of alkaline secondary clays[62], with such regolith-shielding reducing the sensitivity of silicate weathering to temperature change[63]. This mechanism may have reduced the silicate weathering response to warming of the Middle Eocene Climate Optimum (MECO)[5] and possibly the EECO as well[64]. Consequently, the low net silicate weathering may have contributed to elevated CO_2 at the start of the EECO, and the low sensitivity of weathering to temperature change would have made the silicate weathering feedback much slower to act[57]. If so, less complete nutrient consumption in the Southern Ocean, as supported by our observation of elevated $\Delta\delta^{15}N_{SO\text{-}ML}$ during the EECO, could be one of the primary causes for long-lasting high CO_2 of the EECO, triggered by either a reduction in weathering, an increase in geologic CO_2 sources, or a tectonic change encouraging Southern Ocean deep water formation.

Past and future of Southern Ocean biogeochemistry

The amplification of initial warming by a reduction in Southern Ocean biological pump efficiency represents an important positive feedback during the EECO, the capacity of which is greatly enhanced by the reduced buffering capacity of the early Cenozoic ocean (high Ca^{2+} and pCO_2). This Southern Ocean effect is reminiscent of the role it appears to have played in the glacial-interglacial cycles on much shorter timescales[19,30], and potentially capable of acting across other warming intervals, for example the Paleogene hyperthermals and million-year long climate optima such as the Middle Eocene Climate Optima, the Middle Miocene Climate Optimum, and the Pliocene.

The simulated future response of high latitude ocean overturning is uncertain and may change with timescale. In the short term, while strengthening of winds in a warming climate would work to increase overturning[47], freshwater inputs could increase the buoyancy of Antarctic waters, reducing the rates of Antarctic deep water formation[65]. In contrast, simulations

sustained for centuries to thousands of years suggest strengthened Antarctic deep water formation once the deep ocean "catches up" with the warming of the atmosphere and surface ocean[66–68]. This outcome appears to agree with our finding of reduced biological pump efficiency for the EECO, which, in turn, mirrors findings from the glacial-interglacial cycles of the Plio-Pleistocene[3]. The consistency of findings, spanning timescales and boundary conditions, of reduced biological pump efficiency under warm climates supports the likelihood that the Southern Ocean will behave similarly over the longer-term future.

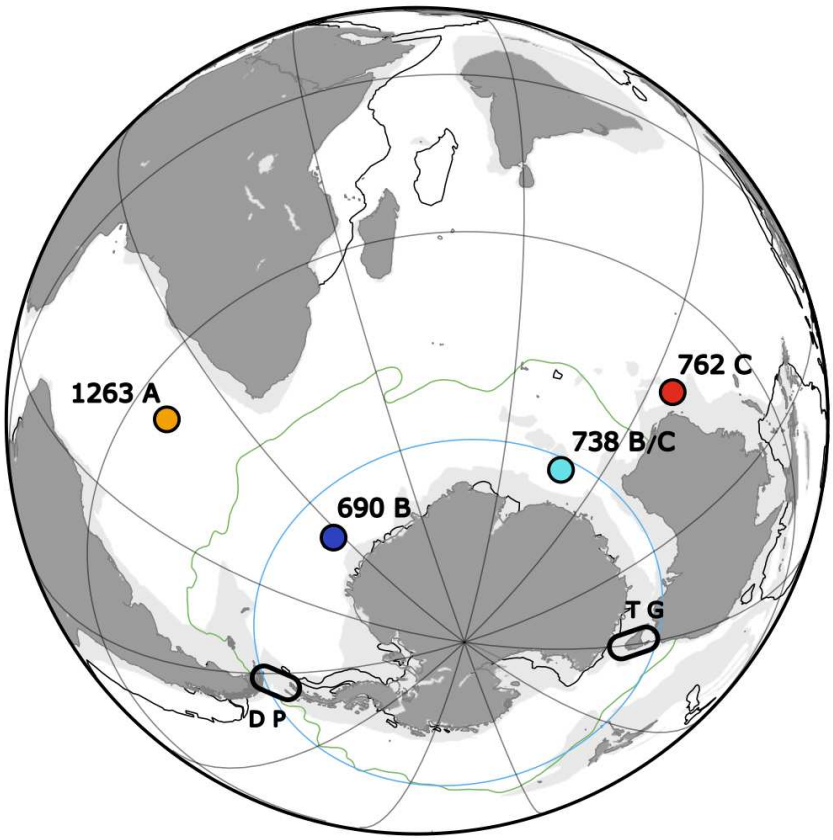

Fig. 1 | Locations of EECO sites investigated in this study on a paleogeographic reconstruction. Circles and numbers depict ODP Site locations for FB-δ^{15}N measurements presented in this work. For the Atlantic, Site 1263 A (yellow) and Site 690B (blue). For the Indian Ocean Site 762C (red) and 738 B/C (light blue). The Map shows a reconstructed paleogeography at 55 Ma on a polar orthographic projection according to a plate rotation model[69]. Site locations are moved consistently within the same model. Green line represents the modern position of the polar front[70]. Black lines represent the position of modern continental outlines. Blue line represents a latitude of 60°S. TG = Tasmanian Gateway. DP = Drake Passage. Both continental gateways have likely been closed at the time of the EECO.

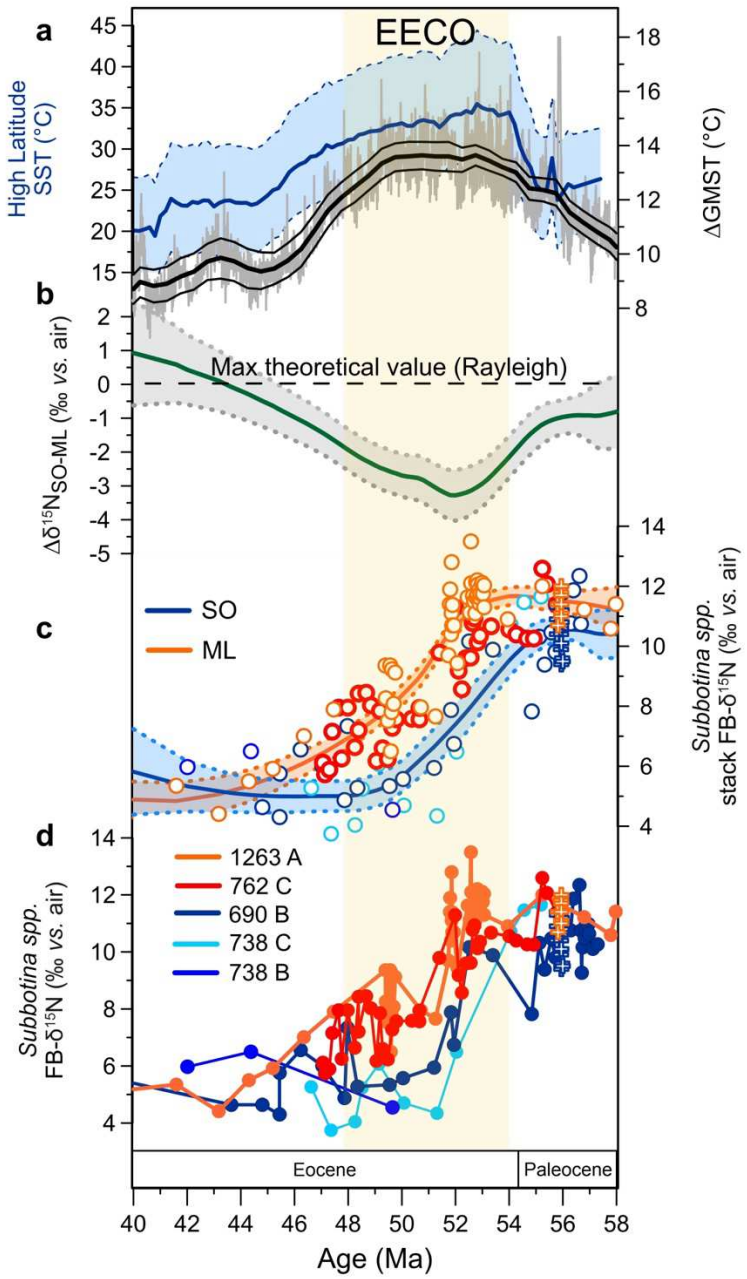

278

279 **Fig. 2 | FB-δ^{15}N and FB-δ^{15}N gradient changes during the EECO. a**, Reconstructed relative
280 global mean surface temperature (GMST) from δ^{18}O records[6] as shown in CenCO$_2$PIP[1]. Black
281 line represents 500-kyr mean Bayesian smoothing (median) with 95% credible intervals.
282 Reconstructed High-Latitude SST from TEX86 with 90% confidence interval[33] (blue). Yellow
283 shading highlights the general EECO warming. **b**, FB-δ^{15}N gradient between the Southern
284 Ocean (SO) and mid-latitude (ML) stacks ($\Delta\delta^{15}N_{SO\text{-}ML}$) from panel c, later used to calculate
285 the degree of nutrient consumption Δf (see Fig. 3). This gradient is proportionate to the degree
286 of nutrient repletion according to a Rayleigh fractionation model. Gray shading represents 95%
287 confidence intervals. **c**, LOESS smoothed stacks of FB-δ^{15}N values of Southern Ocean (SO)

Sites 690 and 738 and mid-latitude (LL) Sites 1263 and 762. Shading represents 95% confidence intervals on the regression for both curves (span=0.75). Crosses represent previously published FB-$\delta^{15}N$ from the Paleocene-Eocene Thermal Maximum in sites 690B and 1263C/D[34] **d,** same data as in c, unsmoothed FB-$\delta^{15}N$ of symbiont-barren foraminifera *Subbotina* sp., colors reflect the relevant DSDP/ODP site (legend). FB-$\delta^{15}N$ measurement precision is ~0.2‰ (1 S.D.).

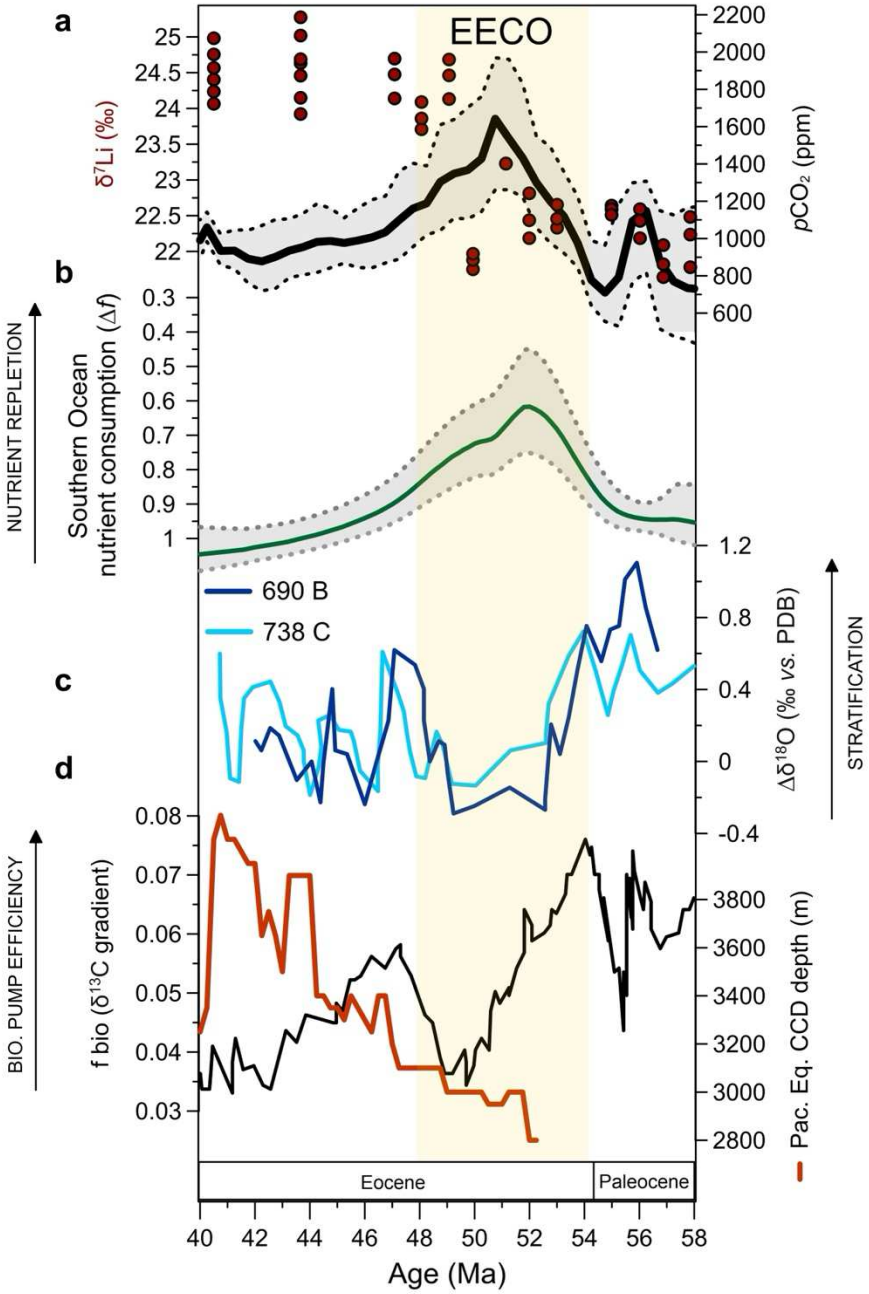

Fig. 3 | Estimated degree of nutrient repletion and comparison with data with independent records of Southern Ocean change. a, foraminifera-δ^7Li (red) weathering proxy[4] and pCO_2 compilation (black) as compiled by CenCO$_2$PIP[1]. Black line represent 500-kyr mean Bayesian smoothing (median), dotted lines with shading depicting credible intervals (95%) for pCO_2 estimates[1]. More positive foraminifera-δ^7Li reflect enhanced incongruent weathering on land. **b,** Computed changes in degree of nutrient consumption Δf applying Rayleigh fractionation model constrained by FB-δ^{15}N gradient ($\Delta\delta^{15}N_{SO\text{-}ML}$) (Fig. 2c). Shading

represents 95% confidence intervals. Note the variable size of the confidence interval, owing to the non-linearity of the Rayleigh fractionation model (see methods). **c,** $\delta^{18}O$ gradients between benthic and planktic foraminifera for Southern Ocean Sites 690 and 738[33]. A reduced vertical gradient is interpreted to reflect a lower stratification of the water column. **d**, Estimated degree of global biological pump efficiency computed from a compilation of benthic and planktic $\delta^{13}C$ values[40] (Black). Reconstructed change in equatorial Pacific carbonate compensation depth (CCD)[71] (Orange).

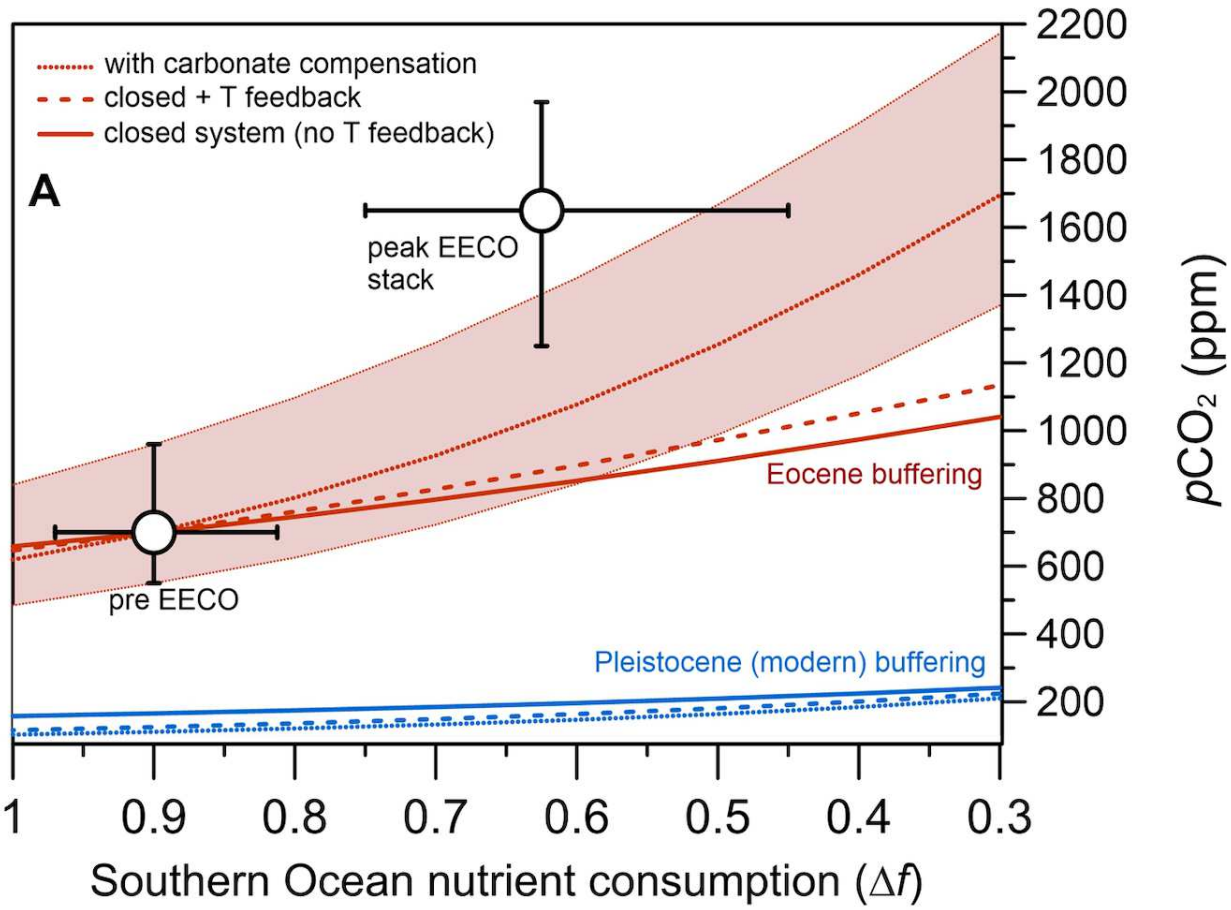

Fig. 4 | Simulated response of atmospheric CO_2 and low-latitude to Southern Ocean degree of nutrient consumption and comparison with observation. Simulations are run with ocean chemistry for the Eocene (red) and Pleistocene (blue) boundary conditions (Methods). Three scenarios are simulated: 1) closed-system (no carbonate compensation) (solid lines), 2) close-system with temperature feedback on Southern Ocean CO_2 release (dashed lines) and 3) open-system (carbonate compensation) including the temperature feedback (dotted lines). White dots with ranges represent observed pCO_2 values (CENCO2PIP)[1] and degree of nutrient consumption Δf (this study) and are based on datasets from Figure 3a and 3b, respectively.

Methods

Core Sites locations

The sediment cores used in this study were collected during various expeditions of the Ocean Drilling Program (ODP). The paleo-geographical locations during the early Eocene (55 Ma) are reported in Fig.1 and Extended Data Table 1. The reconstructions for the EECO continental configuration and the location of study sites are based on the tectonic model of Mueller et al.[69]. Sites 1263 (South Atlantic) and 762 (South Indian Ocean) were located in regions of full nutrient consumption given their position within oligotrophic gyres. Sites 690 and 738 is the Southernmost and highest latitude site in our compilation. At the paleo-locations of Sites 1263 and 762 corresponding to the oligotrophic gyres of present-day ocean, nutrient consumption in the surface waters is expected to have been complete, such that these FB-$\delta^{15}N$ data reflects those of the $\delta^{15}N$ of the deep pycnocline nitrate[25]. Antarctic Sites 690 and 738 did not significantly alter their paleolatitude over the past 60 million years, which constantly remained under –60°S throughout the Cenozoic (Fig.1; Extended Data Table 1).

Age models

Age models for each site are based on combinations of cyclostratigraphic, magnetostratigraphic and biostratigraphic datums (Extended Data Fig. 1). Every magnetostratigraphic and biostratigraphic datum was updated to the latest geochronological timescale GTS 2020[72]. For site 690, the age model is also based on foraminifera and nannofossil biostratigraphy[73] and magnetostragrigraphy[74] from core top down to 135.66 mbsf, and almost exclusively on foraminifera and nannofossil biostratigraphy[73] from 135.66 mbsf later on. A biostratigraphic approach is necessary in the lower part of 690 as it has been shown that magnetostragrigraphy on Maud Rise sites has been diagenetically overprinted in the lower part of the section covering the Paleogene[74]. For sites 738 B and C age model is based on a combination of foraminiferal and nannofossil biostratigraphy for the entire record[75,76]. Site 1263 is based on nannofossil biostratigraphy and magnetostratigraphy[77] in the parts that are not covered by the tuning of isotopic records as discussed in refs.[6,78–80]. Site 762 age model is based biostratigraphy and magnetostratigraphy from Shamrock et al.[81]. The quality of the age model is independently evaluated by stacking benthic $\delta^{18}O$ records of these site from 40 to 60 Ma; evaluating their alignment permit to rule out that the $\Delta\delta^{15}N_{SO\text{-}ML}$ is significantly affected by age model discrepancies (Extended Data Fig. 2).

358 Analysis of foraminifera-bound $\delta^{15}N$

359 Planktonic foraminifera were separated from the sedimentary matrix by wet sieving at
360 63μm and dry-sieving at 150/180 μm. In each sample, around 1000-1500 shells (5-10 mg) of
361 planktonic foraminifera were hand-picked separately under a stereomicroscope for the genus
362 *Subbotina*, the only one present in measurable quantities across all sites. This thermocline-
363 dwelling taxon [82] is dominant in the Southern Ocean Sites 690 and 738, but also present in
364 measurable quantities in mid-latitude Sites 1263 and 762. Briefly, foraminifera shells were
365 crushed in a petri dish before being transferred into a 15 ml conical-base polypropylene tube
366 for cleaning. Samples were treated with a 2% sodium polyphosphate solution adjusted with
367 sodium hydroxide to pH 8 and subsequently rinsed 3 times with milliQ water to remove clay
368 contaminants. Samples were added between 3-7 ml of sodium-dithionite solution (100 ml
369 milliQ, 6.2 g sodium citrate, 2 g sodium bicarbonate, 5 g sodium dithionite, 400 μl 4N NaOH)
370 and placed in a water bath at 80°C for 30 minutes to remove Fe and Mn oxide coatings[83]. The
371 solution was removed, and the samples were rinsed 3 times with milliQ water and transferred
372 into 4 mL glass vials previously muffled at 500°C. A solution of sodium hydroxide and
373 potassium persulfate (2 g recrystallized potassium persulfate, 2 g NaOH, 100 ml milliQ water)
374 was added to the samples, which were subsequently autoclaved at 65 °C for 90 minutes in order
375 to remove all non-shell-bound organics[84,85]. Samples were rinsed 4 times with milliQ water
376 and let dry overnight in an oven at 60 °C. The dissolution of foraminifera mineral matrix and
377 oxidation of the foraminifera-bound organic matter followed the methodology described in
378 Moretti et al.[86]. Between 1 and 5 mg of clean foraminifera carbonate was weighted and
379 transferred into a muffled 4mL vial. 45 μL of 4M hydrochloric acid was added to the samples
380 to dissolve the mineral matrix and expose the proteinaceous content. An oxidizing solution of
381 sodium hydroxide and potassium persulfate (4 ml of 6.25 mol/l NaOH solution, 0.67 g of
382 recrystallized potassium persulfate, 100 ml of milliQ water) was added to each sample, to
383 quantitatively convert organic N to nitrate. Concentration of nitrate was measured for each
384 sample by conversion to nitric oxide followed by the chemiluminescence detection method[87].
385 We did not adjust the pH of our samples as discussed in Ren et al.[84], following the method
386 described in Moretti et al.[86]. Nitrate $\delta^{15}N$ (FB-$\delta^{15}N$) was determined through the denitrifier
387 method[88,89]. Briefly, nitrate samples are quantitatively converted to N_2O by being injected into
388 a gastight vial containing a solution with a strain of the denitrifying bacteria *Pseudomonas*
389 *chlororaphis*, that lacks a functional N_2O reductase. Quantitative conversion of sample nitrate
390 to N_2O was evaluated in each batch together with a series of nitrate standards of known isotopic

composition (IAEA-N3 and USGS-34). The N_2O was extracted, purified, and concentrated by a customized gas-bench ("SigBench") and measured on an online Thermo Scientific MAT253 stable isotope ratio mass spectrometer[89]. The inter-batch precision of two in-house carbonate standards (PO-1 and LO-1) treated with the same method was within 0.2 and 0.1‰ respectively in the range 12-7 nmol, while being 0.3 to 0.5‰ in the 1-6 nmol range. Oxidation blanks were 0.2 nmol of N on average. Foraminiferal organic nitrogen content (nanomole of N per mg of clean foraminifera calcite) is reported in Extended Data Figure 3.

Calculation of nutrient changes

Calculation of changes in nutrient repletion Δf was achieved by numerically approximating the Rayleigh equation with a polynomial function, as this equation does not have an analytical solution. The function can be solved numerically for the degree of nutrient consumption (1-f), which ranges from 0 to a maximum of 1 (oligotrophic conditions). The assumptions discussed in the Main Text allow to estimate the $\delta^{15}N$ of the export production and that of the deep-sourced nitrate from a compilation of Southern Ocean (FB-$\delta^{15}N_{SO}$) and mid-latitude (FB-$\delta^{15}N_{ML}$) oligotrophic sites respectively, and compute f (or its reciprocal 1-f) at any given time (Extended Data Fig. 4).

$$\text{FB-}\delta^{15}N_{SO} \approx \delta^{15}N_{SO} = \delta^{15}N_{deep} + \varepsilon \{f / (1 - f)\} \ln (f) \quad \text{(i)}$$

Mid-latitude oligotrophic sites (FB-$\delta^{15}N_{ML}$) are representative of mean ocean pycnocline $\delta^{15}N$, which in turn is a good approximation of deep ocean $\delta^{15}N$, especially in Eocene ocean configuration (Sijp & England, 2004), where the Southern Ocean's contribution of nitrate to the pycnocline is expected to be low, so that $\delta^{15}N_{deep} \approx$ FB-$\delta^{15}N_{ML}$[35].

$$\Delta\delta^{15}N_{SO\text{-}ML} = \text{FB-}\delta^{15}N_{SO} - \text{FB-}\delta^{15}N_{ML} = \varepsilon \{f / (1 - f)\} \ln (f) \quad \text{(ii)}$$

The value of the isotope effect of nitrate assimilation (ε) is well constrain in the modern Southern Ocean at 5.5‰[24], and it was used for the calculation of f and its variation (Δf).

Numerical simulation

The model architecture is based on Sarmiento & Toggweiler[21], and air-sea CO_2 exchange is implemented using the equations discussed by Sarmiento & Gruber[90] (See Code Availability).

We assume a constant ocean phosphate (PO_4^{3-}) inventory and a fixed phytoplankton biomass C:N:P stoichiometry of 117:16:1. Simulation results represent steady-state solutions. To evaluate the cumulative response of atmospheric CO_2 changes in Southern Ocean nutrient repletion Δf, the model is implemented with and without a temperature feedback responding to simulated CO_2 and with and without a carbonate compensation feedback responding to deep ocean $CaCO_3$ saturation (open system), both induced by the forced changes in Southern Ocean nutrient utilization.

For the temperature feedback, we assume an Earth System Sensitivity (ESS) of 1.5K/W/m^2 and the change in global mean temperature (ΔGMT) caused by changes in CO_2 is thus computed by its radiative forcing (5.35W/m^2 * ln(CO_2/280)) multiplied by ESS[91]. GMT changes are applied to surface ocean temperatures, mainly affecting the solubilities of CO_2 and $CaCO_3$.

$$\Delta_f GMT = ESS * \Delta_f F_{CO_2} = ESS * 5.35 Wm^{-2} * \Delta_f \ln\left(\frac{CO_2}{280\ ppm}\right)$$

$$= ESS * 5.35 Wm^{-2} * k * \overline{N} * \Delta f$$

For $CaCO_3$ compensation, we assume that the ocean achieves steady state mass balance between alkalinity sources from weathering and alkalinity sink from $CaCO_3$ burial when the calcite saturation horizon (CSH) is at a depth of 3000m, following the approach described by Toggweiler[59]. Changes in Southern Ocean nutrient utilization affect the CSH in the closed system simulation (without $CaCO_3$ compensation feedback), while the open system response (open system, compensated scenario) dynamically restores the CSH to its steady state depth of 3000m by changing ALK and total CO_2 in a 2:1 ratio.

To assess the effect of secular changes in seawater composition (i.e., Ca^{2+} and Mg^{2+}) on the sensitivity of CO_2 to Southern Ocean changes, we use the carbonate chemistry and seawater composition described by Hain et al.[9]. For both Pleistocene and Eocene configurations, the model is initialized by prescribing atmospheric pCO_2 (280 and 700ppm, respectively), CSH (3000m in both configurations) and degree of nutrient consumption in the polar ocean (0.1 and 0.9, respectively). Both configurations start with the same total carbon inventories and similar surface calcite saturation (Ω), but the pre-EECO configuration has a significantly lower surface pH supporting the elevated baseline CO_2.

449 The sensitivity of atmospheric CO_2 to imposed changes in polar surface nutrient utilization (Δf)
450 is much greater for Eocene conditions than for the modern/Pleistocene when measured in
451 absolute terms (Extended Data Fig. 5), but a given Δf causes a similar proportional CO_2 change
452 ($\Delta \ln CO_2$) and CO_2 radiative forcing (F_{CO2}) when comparing both scenarios (Extended Data
453 Fig. 6) with and without the temperature and carbonate compensation feedbacks. Therefore,
454 changes in the biological pump retain their strong control on CO_2, global temperatures (GMT)
455 and climate even under elevated Eocene background CO_2 (Extended Data Fig. 6).

456 Statistics and reproducibility

457 Samples were analysed over several batches spanning measurements sessions more than a year
458 apart. Reproducibility given as the s.d. (± 1 s.d.), was within 0.2 ‰ was evaluated with repeated
459 analysis of carbonate biomineral standards presented in Moretti et al.[86]. Isotope analyses
460 performed with MAT253 coupled with a custom-made gas bench (see Analysis of
461 foraminifera-bound $\delta^{15}N$).

462 Data processing for nutrient repletion calculation were conducted using Python (version 3.11)
463 on a Jupyter Notebook (version 7.2.2.). Figures were generated using Grapher version
464 22.1.333. Paleogeographic map was generated using GPlates software (version 2.3.0.)

465 **Data availability**

466 All nitrogen isotope data produced in this study has been uploaded on Zenodo
467 (https://doi.org/10.5281/zenodo.15355111) and will be publicly accessible upon publication.
468 Data is available for reviewers via the following access link:

469 https://zenodo.org/records/15355111?token=eyJhbGciOiJIUzUxMiJ9.eyJpZCI6IjcxMmY5M
470 zlkLWU5YTctNDZkYS1iNWI3LTk4MGNhZjM4MGI1ZCIsImRhdGEiOnt9LCJyYW5kb2
471 0iOiJiODRhMGViNTBiZWFhM2IzZjQ1M2IyZTFhNTg2NjEzMiJ9.me4n01Pyb0fYKn8eL
472 RRUAWqaeF7794JvElNUncLCSoNr7ID4bazJv8t9i9t3tRND_sNZ1GzYLLDXAJt1Dtokgw

473 **Code availability**

474 The code used for calculating the degree of nutrient consumption from nitrogen isotope data is
475 available on GitHub (https://github.com/SimonSaysIsotopes/PaleoNitrate).

The code used for modelling the ocean carbon cycle is available on GitHub (https://github.com/MathisHain/EECO).

Main text references:

1. The cenozoic CO2 proxy integration project (CENCO2PIP) consortium. Toward a Cenozoic history of atmospheric CO2. *Science* **382**, eadi5177 (2023).
2. Hoareau, G. *et al.* Did high Neo-Tethys subduction rates contribute to early Cenozoic warming? *Climate of the Past* **11**, 1751–1767 (2015).
3. Sigman, D. M. *et al.* The Southern Ocean during the ice ages: A review of the Antarctic surface isolation hypothesis, with comparison to the North Pacific. *Quaternary Science Reviews* **254**, 106732 (2021).
4. Misra, S. & Froelich, P. N. Lithium Isotope History of Cenozoic Seawater: Changes in Silicate Weathering and Reverse Weathering. *Science* **335**, 818–823 (2012).
5. Krause, A. J., Sluijs, A., van der Ploeg, R., Lenton, T. M. & Pogge von Strandmann, P. A. E. Enhanced clay formation key in sustaining the Middle Eocene Climatic Optimum. *Nat. Geosci.* **16**, 730–738 (2023).
6. Westerhold, T. *et al.* An astronomically dated record of Earth's climate and its predictability over the last 66 million years. *Science* **369**, 1383–1387 (2020).
7. Tierney, J. E. *et al.* Past climates inform our future. *Science* **370**, (2020).
8. Raymo, M. E. & Ruddiman, W. F. Tectonic forcing of late Cenozoic climate. *Nature* **359**, 117–122 (1992).
9. Hain, M. P., Sigman, D. M., Higgins, J. A. & Haug, G. H. The effects of secular calcium and magnesium concentration changes on the thermodynamics of seawater acid/base chemistry: Implications for Eocene and Cretaceous ocean carbon chemistry and buffering. *Global Biogeochemical Cycles* **29**, 517–533 (2015).
10. Walker, J. C. G., Hays, P. B. & Kasting, J. F. A negative feedback mechanism for the long-term stabilization of Earth's surface temperature. *Journal of Geophysical Research: Oceans* **86**, 9776–9782 (1981).
11. Maher, K. & Chamberlain, C. P. Hydrologic Regulation of Chemical Weathering and the Geologic Carbon Cycle. *Science* **343**, 1502–1504 (2014).
12. Komar, N., Zeebe, R. E. & Dickens, G. R. Understanding long-term carbon cycle trends: The late Paleocene through the early Eocene. *Paleoceanography* **28**, 650–662 (2013).
13. Brune, S., Williams, S. E. & Müller, R. D. Potential links between continental rifting, CO2 degassing and climate change through time. *Nature Geosci* **10**, 941–946 (2017).
14. Lee, C.-T. A. *et al.* Continental arc–island arc fluctuations, growth of crustal carbonates, and long-term climate change. *Geosphere* **9**, 21–36 (2013).

15. Storey, M., Duncan, R. A. & Tegner, C. Timing and duration of volcanism in the North Atlantic Igneous Province: Implications for geodynamics and links to the Iceland hotspot. *Chemical Geology* **241**, 264–281 (2007).
16. Zhang, S.-H., Ji, W.-Q., Chen, H.-B., Kirstein, L. A. & Wu, F.-Y. Linking rapid eruption of the Linzizong volcanic rocks and Early Eocene Climatic Optimum (EECO): Constraints from the Pana Formation in the Linzhou and Pangduo basins, southern Tibet. *Lithos* **446–447**, 107159 (2023).
17. Johnston, F. K. B., Turchyn, A. V. & Edmonds, M. Decarbonation efficiency in subduction zones: Implications for warm Cretaceous climates. *Earth and Planetary Science Letters* **303**, 143–152 (2011).
18. Black, B. A. *et al.* Cryptic degassing and protracted greenhouse climates after flood basalt events. *Nat. Geosci.* **17**, 1162–1168 (2024).
19. Sigman, D. M. & Boyle, E. A. Glacial/interglacial variations in atmospheric carbon dioxide. *Nature* **407**, 859–869 (2000).
20. Ito, T. & Follows, M. J. Preformed phosphate, soft tissue pump and atmospheric CO2. *Journal of Marine Research* **63**, 813–839 (2005).
21. Sarmiento, J. L. & Toggweiler, J. R. A new model for the role of the oceans in determining atmospheric PCO2. *Nature* **308**, 621–624 (1984).
22. Sigman, D. M. & Haug, G. H. The Biological Pump in the Past. *Treatise on Geochemistry* **6**, 625 (2003).
23. Sigman, D. M., Altabet, M. A., McCorkle, D. C., Francois, R. & Fischer, G. The δ15N of nitrate in the southern ocean: Consumption of nitrate in surface waters. *Global Biogeochem. Cycles* **13**, 1149–1166 (1999).
24. Fripiat, F. *et al.* The isotope effect of nitrate assimilation in the Antarctic Zone: Improved estimates and paleoceanographic implications. *Geochimica et Cosmochimica Acta* **247**, 261–279 (2019).
25. Ren, H., Sigman, D. M., Thunell, R. C. & Prokopenko, M. G. Nitrogen isotopic composition of planktonic foraminifera from the modern ocean and recent sediments. *Limnology and Oceanography* **57**, 1011–1024 (2012).
26. Smart, S. M. *et al.* The Nitrogen Isotopic Composition of Tissue and Shell-Bound Organic Matter of Planktic Foraminifera in Southern Ocean Surface Waters. *Geochemistry, Geophysics, Geosystems* **21**, e2019GC008440 (2020).
27. Martínez-García, A. *et al.* Iron Fertilization of the Subantarctic Ocean During the Last Ice Age. *Science* **343**, 1347–1350 (2014).

28. Wang, X. T. *et al.* Deep-sea coral evidence for lower Southern Ocean surface nitrate concentrations during the last ice age. *PNAS* **114**, 3352–3357 (2017).
29. Ai, X. E. *et al.* Southern Ocean upwelling, Earth's obliquity, and glacial-interglacial atmospheric CO2 change. *Science* **370**, 1348–1352 (2020).
30. Sigman, D. M., Hain, M. P. & Haug, G. H. The polar ocean and glacial cycles in atmospheric CO 2 concentration. *Nature* **466**, 47–55 (2010).
31. Hain, M. P. & Sigman, D. M. CO2 in Earth's Ice Age Cycles. in *Oxford Research Encyclopedia of Climate Science* (2024). doi:10.1093/acrefore/9780190228620.013.879.
32. Kast, E. R. *et al.* Nitrogen isotope evidence for expanded ocean suboxia in the early Cenozoic. *Science* **364**, 386–389 (2019).
33. Auderset, A. *et al.* Enhanced ocean oxygenation during Cenozoic warm periods. *Nature* **609**, 77–82 (2022).
34. Moretti, S. *et al.* Oxygen rise in the tropical upper ocean during the Paleocene-Eocene Thermal Maximum. *Science* **383**, 727–731 (2024).
35. Fripiat, F. *et al.* The Impact of Incomplete Nutrient Consumption in the Southern Ocean on Global Mean Ocean Nitrate δ15N. *Global Biogeochemical Cycles* **37**, e2022GB007442 (2023).
36. Thomas, D. J., Bralower, T. J. & Jones, C. E. Neodymium isotopic reconstruction of late Paleocene–early Eocene thermohaline circulation. *Earth and Planetary Science Letters* **209**, 309–322 (2003).
37. Huck, C. E., van de Flierdt, T., Bohaty, S. M. & Hammond, S. J. Antarctic climate, Southern Ocean circulation patterns, and deep water formation during the Eocene. *Paleoceanography* **32**, 674–691 (2017).
38. Sijp, W. P. & England, M. H. Effect of the Drake Passage Throughflow on Global Climate. *Journal of Physical Oceanography* **34**, 1254–1266 (2004).
39. Zhang, Y. *et al.* Early Eocene vigorous ocean overturning and its contribution to a warm Southern Ocean. *Climate of the Past* **16**, 1263–1283 (2020).
40. Hilting, A. K., Kump, L. R. & Bralower, T. J. Variations in the oceanic vertical carbon isotope gradient and their implications for the Paleocene-Eocene biological pump. *Paleoceanography* **23**, (2008).
41. Filippi, G. & Luciani, V. Planktic foraminiferal response to the Early Eocene Climatic Optimum (EECO) from southern mid-to-high latitudes. *Palaeogeography, Palaeoclimatology, Palaeoecology* **659**, 112660 (2025).
42. Schneider, L. J., Bralower, T. J. & Kump, L. R. Response of nannoplankton to early Eocene ocean destratification. *Palaeogeography, Palaeoclimatology, Palaeoecology* **310**, 152–162 (2011).

566 43. Jaccard, S. L., Galbraith, E. D., Martínez-García, A. & Anderson, R. F. Covariation of deep Southern Ocean
567 oxygenation and atmospheric CO2 through the last ice age. *Nature* **530**, 207–210 (2016).
568 44. Hodell, D. A., Venz, K. A., Charles, C. D. & Ninnemann, U. S. Pleistocene vertical carbon isotope and
569 carbonate gradients in the South Atlantic sector of the Southern Ocean. *Geochemistry, Geophysics,*
570 *Geosystems* **4**, 1–19 (2003).
571 45. Toggweiler, J. R., Russell, J. L. & Carson, S. R. Midlatitude westerlies, atmospheric CO2, and climate
572 change during the ice ages. *Paleoceanography* **21**, (2006).
573 46. Gray, W. R. *et al.* Poleward Shift in the Southern Hemisphere Westerly Winds Synchronous With the
574 Deglacial Rise in CO2. *Paleoceanography and Paleoclimatology* **38**, e2023PA004666 (2023).
575 47. Swart, N. C. & Fyfe, J. C. Observed and simulated changes in the Southern Hemisphere surface westerly
576 wind-stress. *Geophysical Research Letters* **39**, (2012).
577 48. Boer, A. M. de, Toggweiler, J. R. & Sigman, D. M. Atlantic Dominance of the Meridional Overturning
578 Circulation. *Journal of Physical Oceanography* **38**, 435–450 (2008).
579 49. Keel, T., Brierley, C., Edwards, T. & Frame, T. H. A. Exploring Uncertainty of Trends in the North Pacific
580 Jet Position. *Geophysical Research Letters* **51**, e2024GL109500 (2024).
581 50. Sigman, D. M., Jaccard, S. L. & Haug, G. H. Polar ocean stratification in a cold climate. *Nature* **428**, 59–63
582 (2004).
583 51. de Boer, A. M. de, Sigman, D. M., Toggweiler, J. R. & Russell, J. L. Effect of global ocean temperature
584 change on deep ocean ventilation. *Paleoceanography* **22**, (2007).
585 52. Roquet, F., Madec, G., Brodeau, L. & Nycander, J. Defining a Simplified Yet "Realistic" Equation of State
586 for Seawater. *Journal of Physical Oceanography* **45**, 2564–2579 (2015).
587 53. Ferreira, D. *et al.* Atlantic-Pacific Asymmetry in Deep Water Formation. *Annual Review of Earth and*
588 *Planetary Sciences* **46**, 327–352 (2018).
589 54. Martin, J. H., Gordon, R. M. & Fitzwater, S. E. Iron in Antarctic waters. *Nature* **345**, 156–158 (1990).
590 55. Martínez-Garcia, A. *et al.* Southern Ocean dust–climate coupling over the past four million years. *Nature*
591 **476**, 312–315 (2011).
592 56. Marinov, I. *et al.* Impact of oceanic circulation on biological carbon storage in the ocean and atmospheric
593 pCO2. *Global Biogeochemical Cycles* **22**, (2008).

57. Hain, M. P., Allen, K. A. & Kirtland Turner, S. Earth system carbon cycle dynamics through time. in *Treatise on Geochemistry (Third edition)* (eds. Anbar, A. & Weis, D.) 381–418 (Elsevier, Oxford, 2025). doi:10.1016/B978-0-323-99762-1.00080-2.
58. Broecker, W. S. & Takahashi, T. The relationship between lysocline depth and *in situ* carbonate ion concentration* †. *Deep Sea Research* **25**, 65–95 (1978).
59. Toggweiler, J. R. Variation of atmospheric CO2 by ventilation of the ocean's deepest water. *Paleoceanography* **14**, 571–588 (1999).
60. Colbourn, G., Ridgwell, A. & Lenton, T. M. The time scale of the silicate weathering negative feedback on atmospheric CO2. *Global Biogeochemical Cycles* **29**, 583–596 (2015).
61. Goddéris, Y., Roelandt, C., Schott, J., Pierret, M.-C. & François, L. M. Towards an Integrated Model of Weathering, Climate, and Biospheric Processes. *Reviews in Mineralogy and Geochemistry* **70**, 411–434 (2009).
62. Moore, J., Lichtner, P. C., White, A. F. & Brantley, S. L. Using a reactive transport model to elucidate differences between laboratory and field dissolution rates in regolith. *Geochimica et Cosmochimica Acta* **93**, 235–261 (2012).
63. Brantley, S. L., Shaughnessy, A., Lebedeva, M. I. & Balashov, V. N. How temperature-dependent silicate weathering acts as Earth's geological thermostat. *Science* **379**, 382–389 (2023).
64. Henehan, M. J. Silicate weathering feedback hindered by clay formation. *Nat. Geosci.* **16**, 663–664 (2023).
65. Bronselaer, B. *et al.* Importance of wind and meltwater for observed chemical and physical changes in the Southern Ocean. *Nature Geoscience* **13**, 35–42 (2020).
66. Yamamoto, A. *et al.* Global deep ocean oxygenation by enhanced ventilation in the Southern Ocean under long-term global warming. *Global Biogeochemical Cycles* **29**, 1801–1815 (2015).
67. Galbraith, E. & de Lavergne, C. Response of a comprehensive climate model to a broad range of external forcings: relevance for deep ocean ventilation and the development of late Cenozoic ice ages. *Clim Dyn* **52**, 653–679 (2019).
68. Frölicher, T. L. *et al.* Contrasting Upper and Deep Ocean Oxygen Response to Protracted Global Warming. *Global Biogeochemical Cycles* **34**, e2020GB006601 (2020).
69. Müller, R. D. *et al.* A Global Plate Model Including Lithospheric Deformation Along Major Rifts and Orogens Since the Triassic. *Tectonics* **38**, 1884–1907 (2019).

70. Orsi, A. H., Whitworth, T. & Nowlin, W. D. On the meridional extent and fronts of the Antarctic Circumpolar Current. *Deep Sea Research Part I: Oceanographic Research Papers* **42**, 641–673 (1995).
71. Pälike, H. *et al.* A Cenozoic record of the equatorial Pacific carbonate compensation depth. *Nature* **488**, 609–614 (2012).
72. *Geologic Time Scale 2020* (eds. Gradstein, F. M., Ogg, J. G., Schmitz, M. D. & Ogg, G. M.) i–iii (Elsevier, 2020). doi:https://doi.org/10.1016/B978-0-12-824360-2.00032-2.
73. *Proceedings of the Ocean Drilling Program, 113 Initial Reports*. vol. 113 (Ocean Drilling Program, 1988).
74. Florindo, F. & Roberts, A. P. Eocene-Oligocene magnetobiochronology of ODP Sites 689 and 690, Maud Rise, Weddell Sea, Antarctica. *GSA Bulletin* **117**, 46–66 (2005).
75. *Proceedings of the Ocean Drilling Program, 119 Scientific Results*. vol. 119 (Ocean Drilling Program, 1991).
76. Huber, B. T. & Quillévéré, F. Revised Paleogene Planktonic Foraminiferal Biozonation for the Austral Realm. (2005).
77. Zachos, J. C. *et al.* Early Cenozoic Extreme Climates: The Walvis Ridge Transect: Covering Leg 208 of the cruises of the Drilling Vessel JOIDES Resolution, Rio de Janeiro, Brazil, to Rio de Janeiro, Brazil, Sites 1262-1267, 6 March-6 May 2003. in *Ocean Drilling Program proceedings. Initial reports* vol. 208 (2004).
78. Rivero-Cuesta, L. *et al.* Paleoenvironmental Changes at ODP Site 702 (South Atlantic): Anatomy of the Middle Eocene Climatic Optimum. *Paleoceanography and Paleoclimatology* **34**, 2047–2066 (2019).
79. Westerhold, T. *et al.* Astronomical calibration of the Ypresian timescale: implications for seafloor spreading rates and the chaotic behavior of the solar system? *Climate of the Past* **13**, 1129–1152 (2017).
80. Westerhold, T. *et al.* Synchronizing early Eocene deep-sea and continental records – cyclostratigraphic age models for the Bighorn Basin Coring Project drill cores. *Climate of the Past* **14**, 303–319 (2018).
81. Shamrock, J. L., Watkins, D. K. & Johnston, K. W. Eocene biogeochronology and magnetostratigraphic revision of ODP Hole 762C, Exmouth Plateau (northwest Australian Shelf). (2012).
82. Pearson, P. N., Shackleton, N. J. & Hall, M. A. Stable isotope paleoecology of middle Eocene planktonic foraminifera and multi-species isotope stratigraphy, DSDP Site 523, South Atlantic. *Journal of Foraminiferal Research* **23**, 123–140 (1993).
83. Mehra, O. P. & Jackson, M. L. Iron oxide removal from soils and clays by a dithionite–citrate system buffered with sodium bicarbonate. in *Clays and Clay Minerals* (ed. Ingerson, E.) 317–327 (Pergamon, 1960). doi:10.1016/B978-0-08-009235-5.50026-7.

84. Ren, H. *et al.* Foraminiferal Isotope Evidence of Reduced Nitrogen Fixation in the Ice Age Atlantic Ocean. *Science* **323**, 244–248 (2009).
85. Nydahl, F. On the peroxodisulphate oxidation of total nitrogen in waters to nitrate. *Water Research* **12**, 1123–1130 (1978).
86. Moretti, S. *et al. Analytical Improvements and Assessment of Long-Term Performance of the Oxidation-Denitrifier Method*. https://essopenarchive.org/users/558394/articles/648017-analytical-improvements-and-assessment-of-long-term-performance-of-the-oxidation-denitrifier-method?commit=bdb84bff3584e165cc9cd8611e61a6dd73b47d4f (2023) doi:10.22541/au.168616993.39320235/v1.
87. Braman, R. S. & Hendrix, S. A. Nanogram nitrite and nitrate determination in environmental and biological materials by vanadium(III) reduction with chemiluminescence detection. *Anal. Chem.* **61**, 2715–2718 (1989).
88. Sigman, D. M. *et al.* A Bacterial Method for the Nitrogen Isotopic Analysis of Nitrate in Seawater and Freshwater. *Anal. Chem.* **73**, 4145–4153 (2001).
89. Weigand, M. A., Foriel, J., Barnett, B., Oleynik, S. & Sigman, D. M. Updates to instrumentation and protocols for isotopic analysis of nitrate by the denitrifier method. *Rapid Communications in Mass Spectrometry* **30**, 1365–1383 (2016).
90. Sarmiento, J. L. & Gruber, N. *Ocean Biogeochemical Dynamics*. (Princeton University Press, 2006).
91. Hain, M. P. & Chalk, T. B. Greenhouse gas effects on Quaternary climates. in *Encyclopedia of Quaternary Science (Third edition)* (ed. Elias, S.) 143–157 (Elsevier, Oxford, 2025). doi:10.1016/B978-0-323-99931-1.00271-3.
92. Mackensen, A. & Ehrmann, W. U. Middle Eocene through Early Oligocene climate history and paleoceanography in the Southern Ocean: Stable oxygen and carbon isotopes from ODP Sites on Maud Rise and Kerguelen Plateau. *Marine Geology* **108**, 1–27 (1992).
93. Kennett, J. P. & Stott, L. D. Proteus and Proto-oceanus: ancestral Paleogene oceans as revealed from Antarctic stable isotopic results: ODP Leg 113. in *Proceedings of the Ocean Drilling Program, Scientific Results* vol. 113 70 (Ocean Drilling Program College Station, Tex, 1990).
94. Barrera, E. & Huber, B. T. Paleogene and early Neogene oceanography of the southern Indian Ocean: Leg 119 foraminifer stable isotope results. *In Barron, J., Larsen, B., et al., Proc. ODP, Sci. Results, 119: College Station, TX (Ocean Drilling Program), 693–717. doi:10.2973/odp.proc.sr.119.167.1991* **119**, (1991).

95. Thomas, E. Cenozoic Deep-Sea Circulation: Evidence from Deep-Sea Benthic Foraminifera. in *The Antarctic Paleoenvironment: A Perspective on Global Change: Part One* 141–166 (American Geophysical Union (AGU), 1992). doi:10.1029/AR056p0141.

96. Stap, L., Lourens, L., van Dijk, A., Schouten, S. & Thomas, E. Coherent pattern and timing of the carbon isotope excursion and warming during Eocene Thermal Maximum 2 as recorded in planktic and benthic foraminifera. *Geochem. Geophys. Geosyst.* **11**, Q11011 (2010).

97. Lauretano, V., Littler, K., Polling, M., Zachos, J. C. & Lourens, L. J. Frequency, magnitude and character of hyperthermal events at the onset of the Early Eocene Climatic Optimum. *Climate of the Past* **11**, 1313–1324 (2015).

98. Lauretano, V., Zachos, J. C. & Lourens, L. J. Orbitally Paced Carbon and Deep-Sea Temperature Changes at the Peak of the Early Eocene Climatic Optimum. *Paleoceanography and Paleoclimatology* **33**, 1050–1065 (2018).

99. McCarren, H., Thomas, E., Hasegawa, T., Röhl, U. & Zachos, J. C. Depth dependency of the Paleocene-Eocene carbon isotope excursion: Paired benthic and terrestrial biomarker records (Ocean Drilling Program Leg 208, Walvis Ridge). *Geochemistry, Geophysics, Geosystems* **9**, (2008).

100. Thomas, E. *et al.* Early Eocene Thermal Maximum 3: Biotic Response at Walvis Ridge (SE Atlantic Ocean). *Paleoceanography and Paleoclimatology* **33**, 862–883 (2018).

Acknowledgements: We are grateful to Mareike Schmitt, Florian Rubach, and Barbara Hinnenberg for assistance in the laboratory. This work was funded by the Max Planck Society (MPG). DMS received support from the Tuttle Fund of the Department of Geosciences at Princeton University. S.M. acknowledges funding from the German Research Foundation (DFG 529282003).

Author contributions: S.M. and F.F designed the study. S.M. measured foraminifera bound nitrogen isotopes and wrote the first draft of the manuscript and all co-authors contributed significantly to the following iterations. S.M., F.F and M.P.H. worked on the numerical simulation of Southern Ocean biogeochemistry. A.M.G., G.H.H., R.S., and D.M.S. obtained funding and contributed resources for this project. L.L., T.A., V.L., G.F. helped with sample preparation. L.G. and P.B. contributed to the foraminifera classification and paleoecology under the supervision of R.S. All authors contributed to the interpretation of the data and the writing of the manuscript.

Competing interests: The authors declare no competing interests.

Material and correspondence: correspondence and requests for materials should be addressed to simone.moretti@mpic.de or a.martinez-garcia@mpic.de.

Extended data:

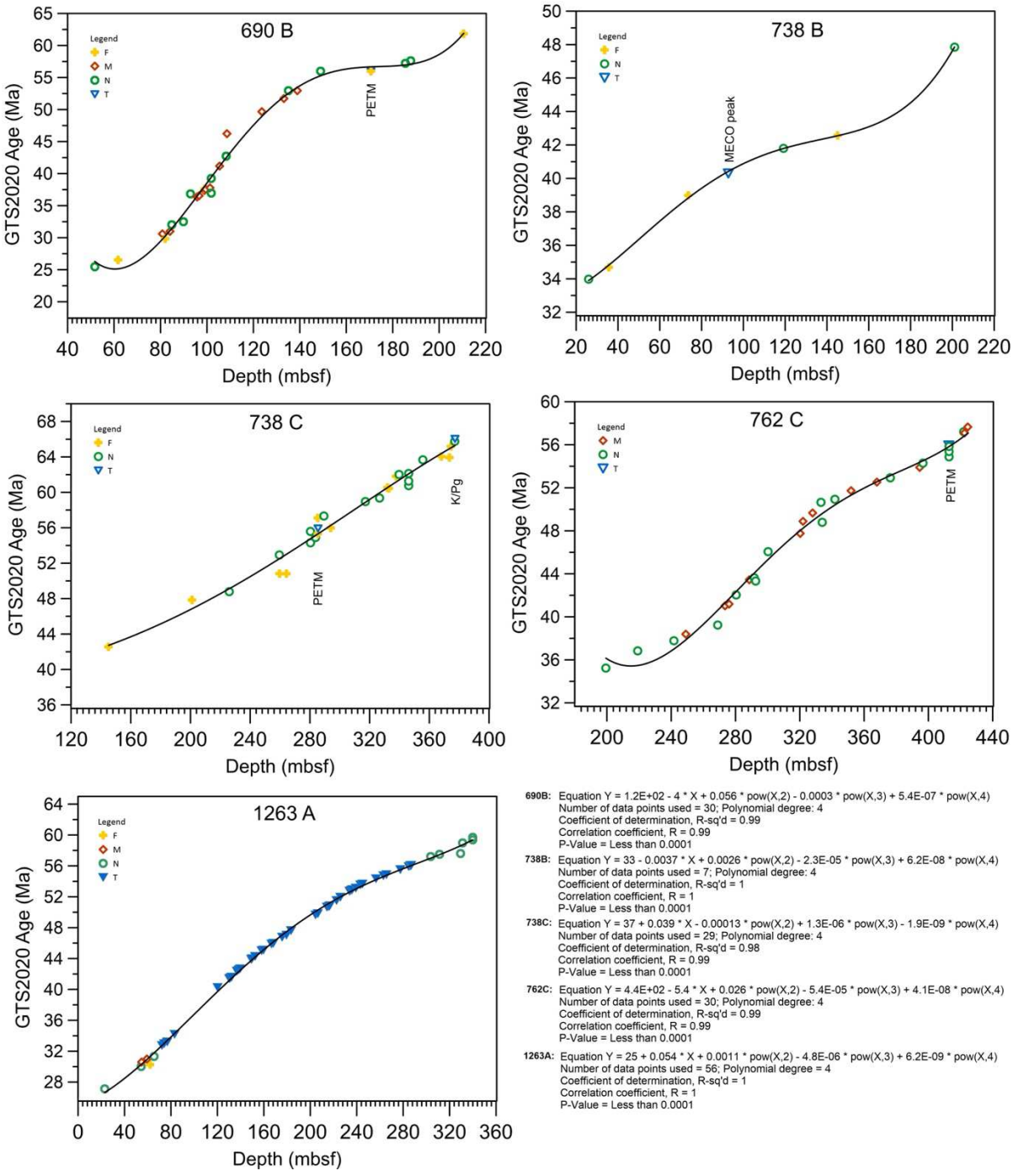

Extended Data Figure 1| GTS2020-adjusted age models. a, Site 690B (refs.[73,74]). **b**, Site 738B (refs.[75,76]). **c**, Site 738C (refs.[75,76]). **d**, Site 762C (ref.[81]). **e**, Site 1263A (refs.[6,77–79]). F is foraminifera biostratigraphy, M is magnetostratigraphy, N is nannofossil biostratigraphy and T are tiepoints based isotopic excursions. A fourth-degree polynomial fit was chosen for all age models (P-Value < 0.0001 in all cases).

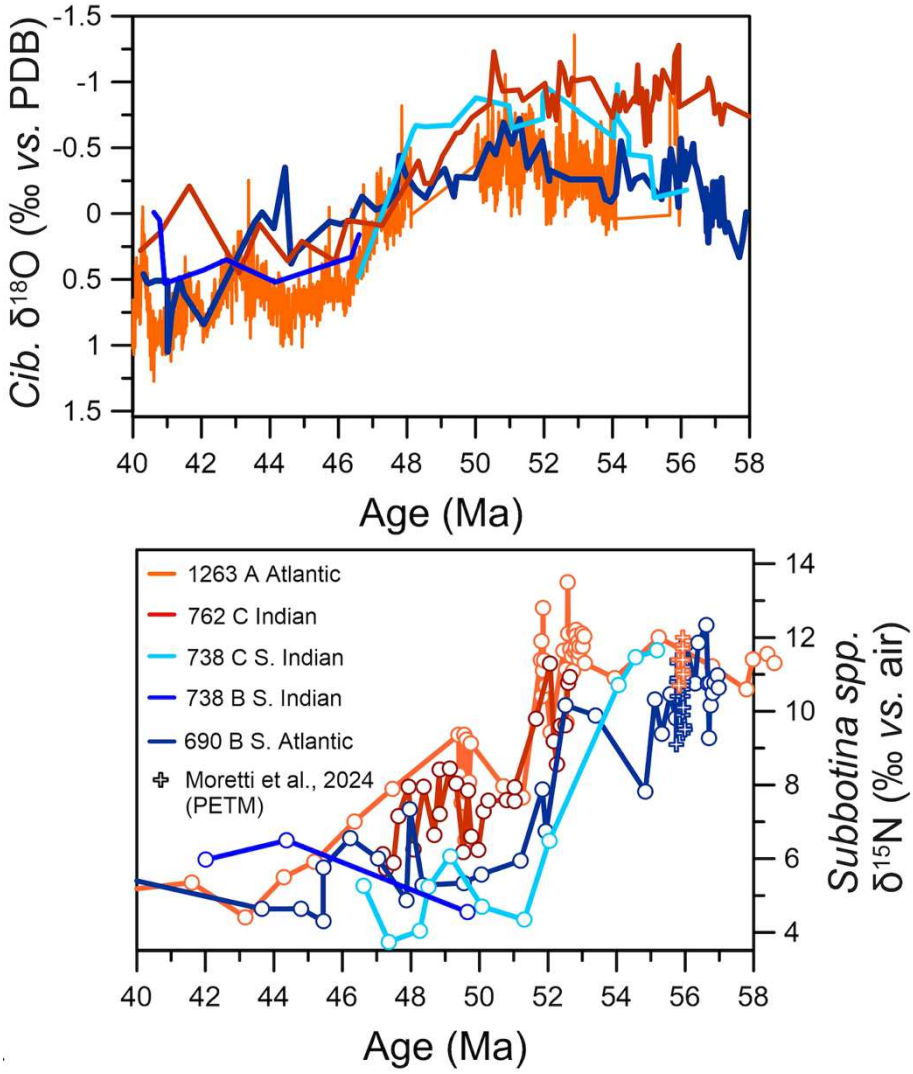

Extended Data Figure 2 | Stable isotope records of oxygen and nitrogen for the sites examined in this study. Alignment of $\delta^{18}O$ records is used to independently evaluate the quality of the age models (Extended Data Fig. 1) after the bio- and magnetostratigraphic tie points that constitute the individual age models have all been recalibrated to the same geochronological timescale (GTS2020). $\delta^{18}O$ records for Site 690 (refs.[92,93]), Sites 738 B and C (ref.[94]), 762C (ref.[95]) and 1263 A/B/C (refs. [6,80,96–100]).

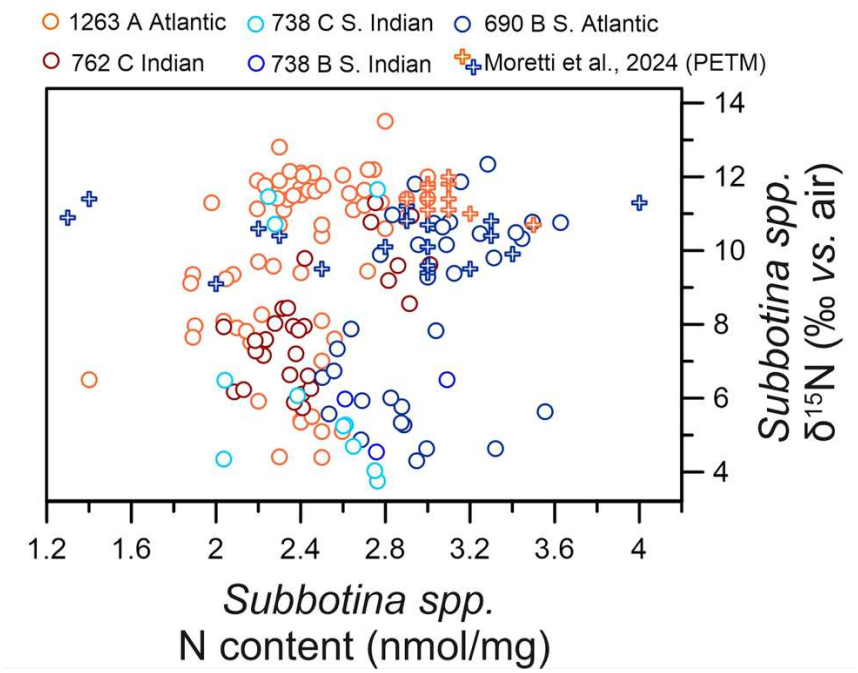

734
735

736 **Extended Data Figure 3 | Crossplot of stable isotopes of nitrogen content and nitrogen**
737 **isotopic composition of Palegoene subbotinids.**

738

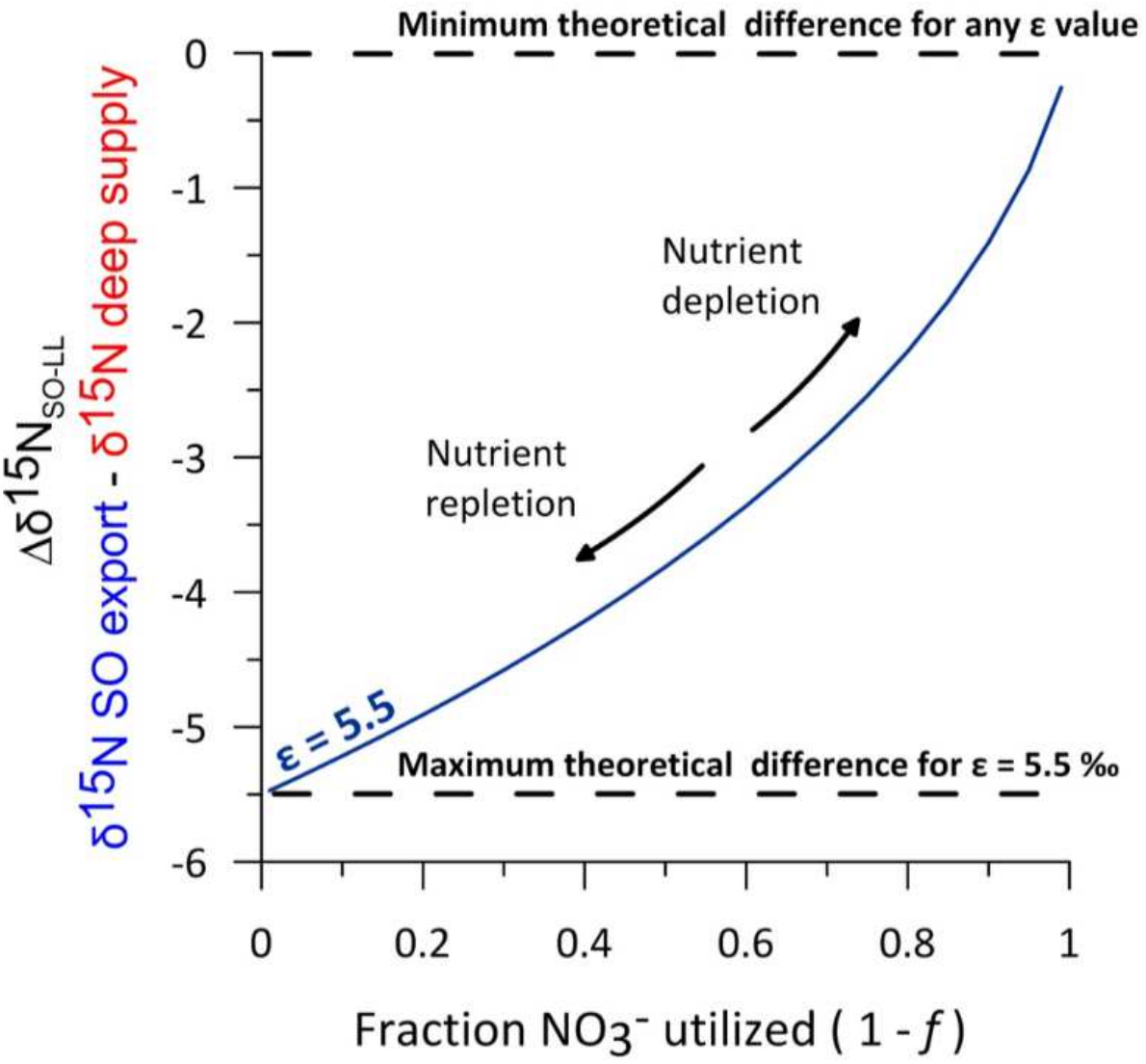

Extended Data Figure 4 | Rayleigh model for estimating the degree of nutrient consumption in the Southern Ocean from $\Delta\delta^{15}N_{SO\text{-}ML}$. The Difference $\Delta\delta^{15}N_{SO\text{-}ML}$ is calculated between measured FB-δ^{15}N in *Subbotina spp.* high-latitude Southern Ocean sites (estimation of δ^{15}N of high-latitude export production) and FB-δ^{15}N in *Subbotina spp.* mid-latitude sites (oligotrophic, estimation of δ^{15}N of deep water nitrate supply). The $\Delta\delta^{15}N_{SO\text{-}ML}$ gradient is a function of the fraction of nutrient utilized (1-*f*).

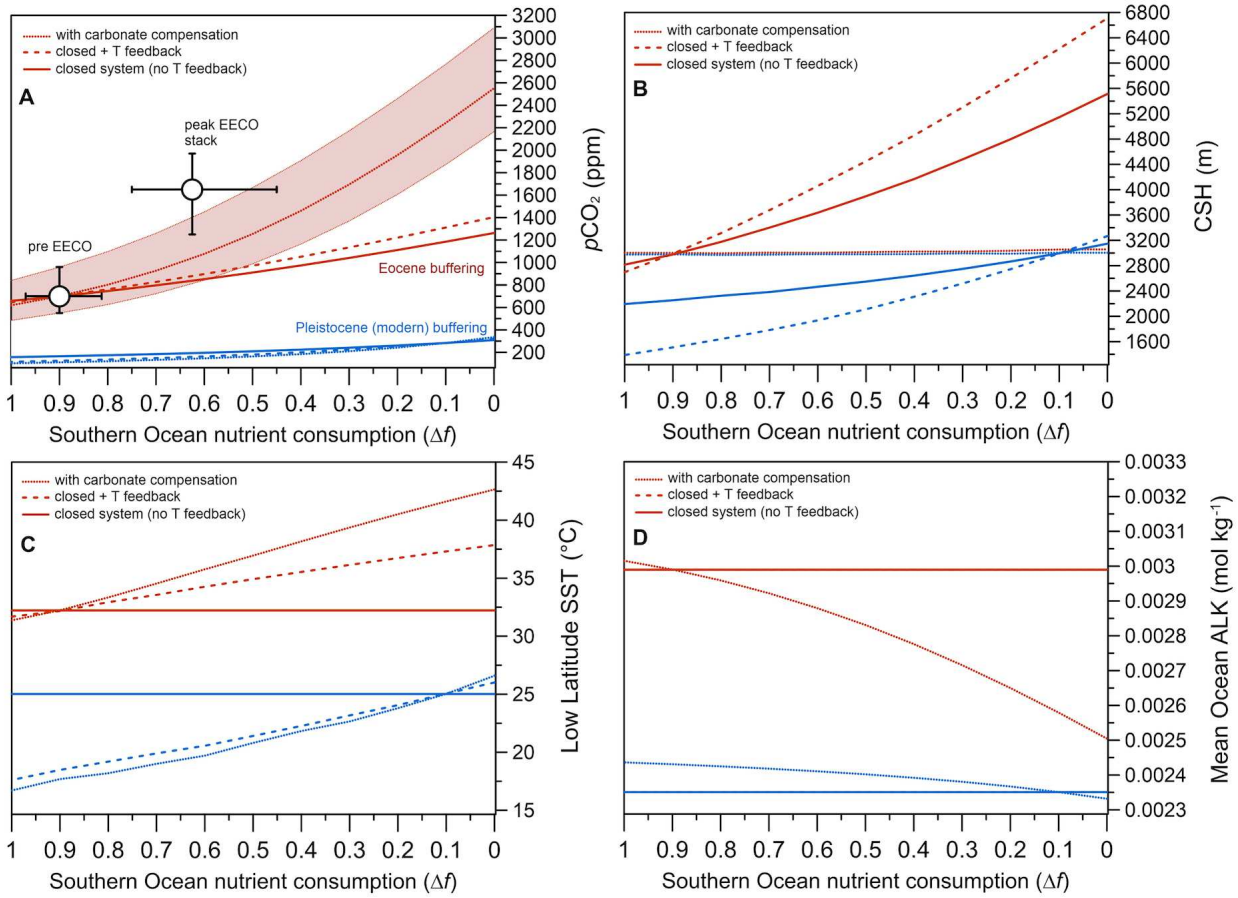

Extended Data Figure 5 | Simulation results for carbon cycle variables. The response of the carbon cycle variables to Southern Ocean degree of nutrient consumption for the Eocene (red) and Pleistocene (blue) boundary conditions. (A) atmospheric CO_2 as shown in Figure 4 (main text) (B) low latitude sea surface temperature (SST), (C) Carbonate saturation horizon (CSH) and (D) whole-ocean alkalinity (ALK). Three scenarios are simulated: 1) closed-system (no carbonate compensation) (solid lines), 2) open-system without temperature feedback (dashed lines) and 3) open-system including temperature feedback (dotted lines).

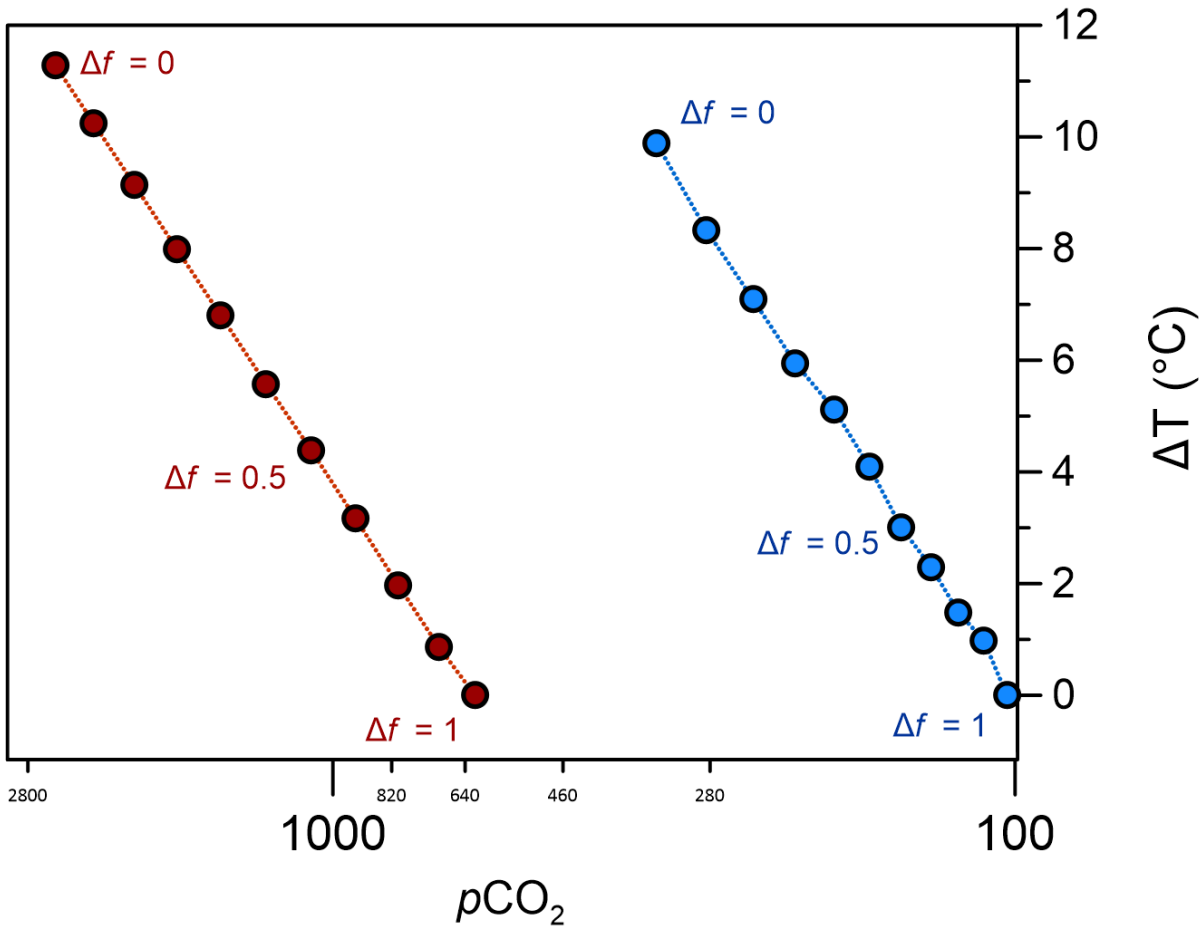

757

758 **Extended Data Figure 6 | Linear relation between pCO_2 (log scale) and temperature**
759 **change evaluated for different degree of nutrient consumption in the Southern Ocean Δ*f*.**
760 The model implements and Earth System Sensitivity (ESS) of 1.5K/W/m^2 and the radiative
761 forcing $RCO_2 = 5.35$ W/m^2 $\times \ln(pCO_2/C_0)$ where C_0 is pre-industrial CO_2 concentration (~280
762 ppm). Note that both Pleistocene (blue) and Eocene (red) have the same sensitivity despite the
763 different ocean chemistries (buffering capacity).

764

765

Expedition	Site/Hole	Basin	Modern lat.	Modern long	Paleolat.	Paleolong.
ODP 119	738 B/C	Indian	–62.709	82.788	–62.44	75.64
ODP 143	762 C	Indian	–19.887	112.254	–43.23	95.23
ODP 208	1263 A/D	Atlantic	–28.533	2.778	–36.16	–11.80
ODP 113	690 B	Atlantic	–65.15	1.2	–65.96	–6.27

766

767 **Extended Data Table 1 | Sites used for FB-δ^{15}N in this study.** Paleolatitude reconstructed

768 with tectonic modelling from Müller et al.[69] at 55 Ma as shown in Fig. 1 (Main Text).

769